The convergence of head-on DNA unwinding forks induces helicase oligomerization and activity transition

Lulu Bi, Zhenheng Qin, Teng Wang, Yanan Li, Xinshuo Jia, Xia Zhang, Xi-Miao Hou, Mauro Modesti, Xu-Guang Xi, Bo Sun

PNAS RESEARCH ARTICLE | BIOPHYSICS AND COMPUTATIONAL BIOLOGY

The convergence of head-on DNA unwinding forks induces helicase oligomerization and activity transition

Lulu Bi[a,1], Zhenheng Qin[a,b,c,1,2], Teng Wang[a], Yanan Li[a], Xinshuo Jia[a], Xia Zhang[a], Xi-Miao Hou[d], Mauro Modesti[e], Xu-Guang Xi[f], and Bo Sun[a,3]

Edited by Stephen West, The Francis Crick Institute, London, United Kingdom; received September 26, 2021; accepted April 19, 2022

Helicases are multifunctional motor proteins with the primary task of separating nucleic acid duplexes. These enzymes often exist in distinct oligomeric forms and play essential roles during nucleic acid metabolism. Whether there is a correlation between their oligomeric state and cellular function, and how helicases effectively perform functional switching remains enigmatic. Here, we address these questions using a combined single-molecule approach and Bloom syndrome helicase (BLM). By examining the head-on collision of two BLM-mediated DNA unwinding forks, we find that two groups of BLM, upon fork convergence, promptly oligomerize across the fork junctions and tightly bridge two independent single-stranded (ss) DNA molecules that were newly generated by the unwinding BLMs. This protein oligomerization is mediated by the helicase and RNase D C-terminal (HRDC) domain of BLM and can sustain a disruptive force of up to 300 pN. Strikingly, onsite BLM oligomerization gives rise to an immediate transition of their helicase activities, from unwinding dsDNA to translocating along ssDNA at exceedingly fast rates, thus allowing for the efficient displacement of ssDNA-binding proteins, such as RPA and RAD51. These findings uncover an activity transition pathway for helicases and help to explain how BLM plays both pro- and anti-recombination roles in the maintenance of genome stability.

BLM | helicase | oligomerization | single molecule | SSB

Significance

Bloom syndrome helicase (BLM) is a multifunctional helicase that primarily catalyzes the separation of two single strands of DNA. Here, using a single-molecule optical tweezers approach combined with confocal microscopy, we monitored both the enzymatic activity and oligomeric status of BLM at the same time. Strikingly, a head-on collision of BLM-medicated DNA unwinding forks was found to effectively switch their oligomeric state and activity. Specifically, BLMs, upon collision, immediately fuse across the fork junctions and covert their activities from dsDNA unwinding to ssDNA translocation and protein displacement. These findings explain how BLM plays multiple functional roles in homologous recombination (HR). The single-molecule approach used here provides a reference model for investigating the relationship between protein oligomeric state and function.

Helicases are ubiquitous molecular motors found in all organisms, from phages to humans (1). These enzymes typically use the chemical energy from nucleoside triphosphate binding and hydrolysis to catalyze the strand separation of the duplex form of nucleic acids and participate in almost every aspect of DNA and RNA metabolism (2–4). Moreover, increasing evidence suggests that DNA helicases are multifunctional enzymes, and besides DNA unwinding, they play additional roles in DNA replication, repair, and recombination, such as protein displacement from DNA and structural rearrangement of protein complexes (4–7). However, little is known about how helicases effectively achieve the functional switching.

Notably, DNA helicases often realize specific functions in distinct oligomeric species (7–9). For instance, some helicases from superfamilies 1 and 2 (e.g., UvrD) can translocate along single-stranded (ss) DNA as monomers but unwind double-stranded (ds) DNA as dimers (10–13). It is widely appreciated that the self-association of proteins to form dimers or higher-order oligomers confers structural and functional advantages and acts as a key factor in the regulation of protein (14). Thus, it is plausible that a multifunctional helicase may switch cellular functions through the autonomous adjustment of its oligomeric state. One of the impediments to testing the hypothesis is the relative paucity of biophysical methods that allow for the simultaneous detections of both the oligomeric state and the function of the examined enzyme.

In this work, we investigated the functional switch pathway for the Bloom syndrome helicase (BLM) at the single-molecule level. BLM, one of the highly conserved RecQ family enzymes, is a model helicase that has proven to unwind duplex DNA in its monomeric form (15, 16). BLM can also form other oligomeric species, such as dimer and hexamer, whereas their corresponding cellular functions remain largely unknown (17, 18). In addition to unwinding dsDNA, the BLM can process other distinctive DNA substrates, recruit and displace partner proteins, and stimulate and suppress their enzymatic activities, acting as a multifunctional "caretaker" for genome stability (16, 19).

Herein, we developed a single-molecule optical tweezers approach combined with confocal microscopy to examine the consequence of a head-on collision of BLM-mediated unwinding forks. We found that the convergence of DNA unwinding forks mediated by the BLMs leads to onsite protein oligomerization. In addition, their enzymatic activities were correspondingly converted from dsDNA unwinding to ssDNA-binding protein

Author contributions: B.S. designed research; L.B. and Z.Q. performed research; T.W., Y.L., X.J., X.Z., X.-M.H., M.M., X.-G.X., and B.S. contributed new reagents/analytic tools; L.B., Z.Q., and B.S. analyzed data; and L.B. and B.S. wrote the paper.

The authors declare no competing interest.

This article is a PNAS Direct Submission.

[1]L.B. and Z.Q. contributed equally to this work.

[2]Present address: Institute of Molecular Medicine, Renji Hospital, School of Medicine, Shanghai Jiao Tong University, Shanghai 200127, China.

[3]To whom correspondence may be addressed. Email: sunbo@shanghaitech.edu.cn.

This article contains supporting information online at http://www.pnas.org/lookup/suppl/doi:10.1073/pnas.2116462119/-/DCSupplemental.

Published June 3, 2022.

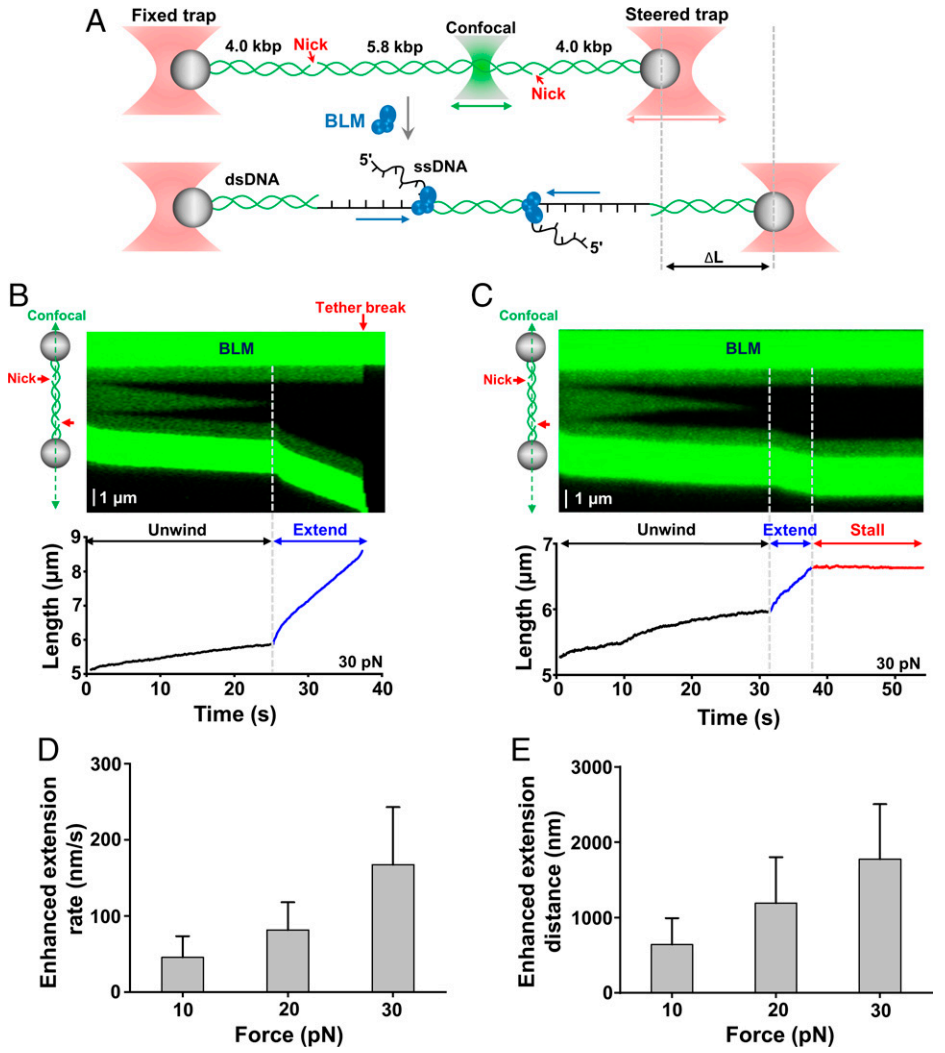

Fig. 1. Experimental configuration and BLM-mediated unwinding of a double-nicked DNA template. (*A*) Schematic of the experimental configuration. Biotinylated double-nicked DNA was suspended between two streptavidin-coated beads that were manipulated by a fixed and a steered optical trap. Meanwhile, a confocal laser was repeatedly scanned along the DNA template. DNA length is expected to increase under a constant force higher than 6 pN when dsDNA is unwound to ssDNA by BLM. The blue arrows indicate the directions of BLM motions. (*B*) A representative kymograph of a double-nicked DNA and its corresponding DNA length as a function of time in the presence of 200 nM BLM under 30 pN. The dsDNA unwinding (black) is followed by the enhanced DNA extension (blue). The vertical dotted line indicates the transition of the enzymatic activities. (*C*) A representative kymograph of a double-nicked DNA as well as its corresponding DNA length as a function of time in the presence of 200 nM BLM under 30 pN. After dsDNA unwinding (black), the enhanced DNA extension (blue) is followed by a long stall (red). (*D* and *E*) Enhanced DNA extension rate in nm/s and distance in nm in the presence of 200 nM BLM under 10, 20, and 30 pN. The error bars represent SD.

(SSB) displacement. Overall, our work not only determines a distinct function of the oligomeric BLM, but also unveils an activity transition pathway for helicase. These findings help to better understand BLM's multifunctional roles in the maintenance of genome integrity and stability.

Results

The Convergence of Head-On DNA Unwinding Forks Gives Rise to a Sudden Increase in DNA Extension Rate. To examine the outcome of meeting unwinding BLMs on a single DNA molecule, we constructed a 13.8-kbp DNA substrate harboring two nicks on two different strands located 4.0 kbp away from each 5′ end (Fig. 1*A* and *SI Appendix*, Fig. S1). Since BLM prefers to translocate on intact ssDNA in a 3′ to 5′ manner when initiating unwinding from a nick (20), two nick-initiated unidirectional unwinding events of this DNA template would result in a convergence of head-on unwinding forks between the nicks (Fig. 1*A*). In our assay, this specifically designed DNA molecule was suspended between two optical traps while a confocal laser repeatedly scanned along the plane of the DNA template. A high-frequency feedback system on the steered trap ensures that the force on the template remains constant (Fig. 1*A*). Helicase unwinding would result in an increase in DNA length under a relatively high force (*SI Appendix*, Fig. S2) as well as an immediate dissociation of the fluorescent agent Sytox for dsDNA, permitting simultaneous tracking of helicase motion and DNA intermediates during unwinding (Fig. 1*A*).

To ensure that two dsDNA unwinding events initiated from both nicks occur simultaneously and with processivity, we carried out experiments with 200 nM of a helicase-core fragment of *Gallus gallus* BLM (gBLM-core, hereafter referred to as gBLM) and 2 mM adenosine triphosphate (ATP). Under 30 pN of assisting force, the kymographs and the increases in DNA length demonstrated that two head-on unwinding events that were initiated from the designed nicks occurred in all 34 examined templates and progressed smoothly at an overall rate of 26 ± 7 nm/s (Fig. 1 *B* and *C*), corresponding to 183 ± 50 bp/s for both events (*SI Appendix*, Figs. S2 and S3*A*). However, surprisingly, rather than DNA tether breakage, the completion

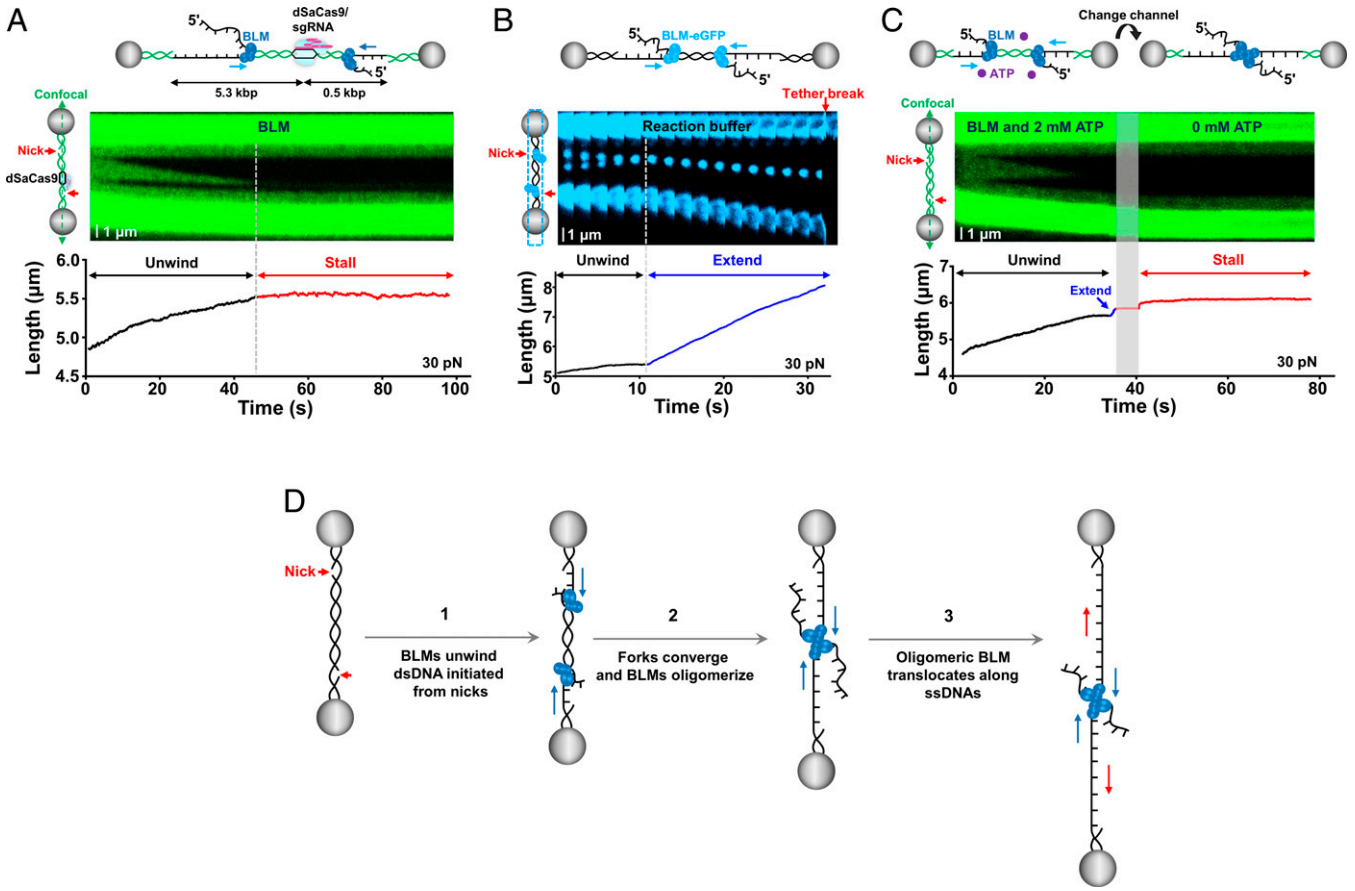

Fig. 2. BLM oligomerization at the converged forks and the ATPase activity of the oligomeric BLM. (*A*) A representative kymograph of a double-nicked DNA bound by a dSaCas9/sgRNA complex between two nicks and its corresponding DNA length as a function of time in the presence of 200 nM BLM under 30 pN. The DNA extension rate transition is not detected, but a long stall is instead. (*B*) A representative kymograph of a double-nicked DNA as well as its corresponding length as a function of time in the presence of BLM-eGFP. The dsDNA unwinding was initiated in a channel containing 200 nM BLM-eGFP, after which the tether was transported to the reaction buffer. BLM-eGFP proteins are indicated in cyan. (*C*) Representative kymograph and DNA length versus time trace of a double-nicked DNA showing dsDNA unwinding initiating in a channel containing 200 nM BLM under 30 pN, followed by quick transport to a channel containing the reaction buffer without ATP (gray rectangle). In this channel, a long pause was detected. (*D*) A functional switching model of the BLM. The oligomerization of the unwinding BLMs at the fork junctions switches their activities from dsDNA unwinding to ssDNA translocation. The blue arrows indicate the directions of BLM motions. The red arrows indicate the directions of the translocation of two ssDNA molecules. For clarity, only one BLM across each fork junction is shown in the cartoon.

of the unwinding of the 5.8-kbp dsDNA between two nicks, corresponding to a 0.83-μm increase in DNA extension under 30 pN (*SI Appendix*, Figs. S2 and S3*B*), gave rise to a sudden enhancement of the DNA extension rate to 167 ± 76 nm/s (Fig. 1*B*–*D*). Then, the enhanced rates were maintained until tether breakage ($n = 18$) (Fig. 1*B*) or interruption by long-standing stalls (over 120 s) ($n = 16$) (Fig. 1*C*). Control experiments verified that the detected sudden transition is independent of Sytox used in the assay (*SI Appendix*, Fig. S4). Enhanced DNA extension rates were also detected under external forces of 10 and 20 pN (*SI Appendix*, Fig. S5). The statistics showed that both the DNA extension rate and processivity (defined as the DNA extension between the rate transition point and tether breakage or stall) after the transition were enhanced by the increased force (Fig. 1 *D* and *E* and *SI Appendix*, Fig. S5). In addition, we demonstrated similar rate transitions with wild-type (WT) BLM and a core fragment of human BLM (hBLM-core, hereafter referred to as hBLM), indicating that this transition is a conserved characteristic of the BLM (*SI Appendix*, Figs. S6 and S7).

Enhanced DNA Extension Arises from BLM Oligomerization and ssDNA Translocation of the Oligomeric BLM. We next aimed to unveil the origin of the sudden enhancement of the DNA extension rate mediated by BLM. The rate transition occurring at the unwinding fork convergence motivated us to speculate that it might arise from the forgathering and oligomerization of the unwinding BLMs. To test this hypothesis, we first preassociated a dead version of Cas9 from *Staphylococcus aureus* (dSaCas9) complexed with a single-guide RNA (sgRNA) on the dsDNA located 5.3 and 0.5 kbp away from the two nicks, respectively (Fig. 2*A*). The DNA-bound dSaCas9-sgRNA complex serves as a strong roadblock to prevent the convergence of the two unwinding forks and, thus, the direct interaction between unwinding BLMs (21). The kymograph of the DNA template indicated successive stalls (over 60 s) of the two unwinding events at the dSaCas9/sgRNA binding site (Fig. 2*A*). No rate transitions were detected in any of the 11 traces examined. These data strongly suggest that the rate transition, indeed, relies on fork convergence and direct contacts among BLMs, which is possibly realized by the oligomerization of the unwinding BLMs right across the fork junctions.

To directly monitor the motion and oligomeric state of BLM, we revisited the DNA unwinding assay with enhanced green fluorescent protein–labeled BLM (BLM-eGFP). To better illustrate the fluorescent signal, DNA unwinding, once initiated in a BLM-eGFP-containing channel, was immediately transported and monitored in a protein-free channel with

confocal laser scanning of a rectangular area rather than the DNA track (Fig. 2*B*). In all 23 examined DNA templates, two groups of BLMs at the two DNA unwinding forks were monitored to move smoothly in a head-on manner before fork convergence, while DNA length increased at a relatively slow rate. The fluorescence intensity of BLM-eGFP indicates that more than one BLM appeared around each unwinding fork (see *Discussion*). As expected, a similar rate transition was also detected with BLM-eGFP, and its occurrence was, indeed, accompanied by the two groups of BLMs meeting in the middle of the template (Fig. 2*B*). Notably, during the enhanced DNA extension, the two groups of BLMs stayed together and moved to maintain the middle position along the continuously extended DNA tether without dissociation. These data corroborate that the rate transition is, indeed, a result of BLM oligomerization across the forks.

We further addressed whether the enhanced DNA extension is dependent on the ATPase activity of BLM. To this aim, we conducted a BLM unwinding experiment in one channel containing 200 nM BLM and 2 mM ATP to ensure the fork convergence and rate transition. Following the transition, we rapidly transferred the DNA tether to a reaction buffer channel without ATP. In this channel, the enhanced DNA extensions were immediately abolished, and long pauses were detected instead in 19 examined tethers (Fig. 2*C*). Thus, the enhanced DNA extension is a result of the ATPase activity of BLM.

How was the DNA extension rate suddenly increased? First, the kymograph displayed the progression of the dark region during the enhanced DNA extension process, indicating the emergence of the newly generated ssDNA between two traps (Fig. 1 *B* and *C*). Second, several helicases, in addition to DNA unwinding, are well known to be able to translocate on ssDNA, the rates of which are often significantly faster than the rates of dsDNA unwinding (22, 23). Based on the assumption that the expanded dark region represents ssDNA, the enhanced rate under 30 pN (167 ± 76 nm/s) (Fig. 1*D*) was estimated to be 327 ± 148 nt/s, which is 1.8-fold faster than the unwinding rate (*SI Appendix*, Figs. S3 and S5). Third, after the rate transition, the maximal DNA extension length can reach up to 2.89 μm under 30 pN ($n = 8$) and 2.45 μm under 20 pN ($n = 5$), approximately the length of the newly generated 5.8-knt ssDNA under each force (*SI Appendix*, Fig. S5). These analyses strongly suggest that the enhanced DNA extension is highly likely due to the translocation of the oligomeric BLM along two coiled ssDNAs, leading to the transition of coiled ssDNAs to tensioned ssDNAs between two optical traps (Fig. 2*D*).

Collectively, we attributed the detected rate transition to BLM oligomerization upon fork convergence and functional switching from unwinding dsDNAs to translocating along ssDNAs (Fig. 2*D*). One of the explanations for the stochastically stalled translocation could be the tangled ssDNA that prevents the oligomeric BLM from further movement. It is not escaping our notice that the translocations of two ssDNAs were always stalled at the same time, suggesting coincident activity of the BLMs within the oligomer.

The HRDC Domain of BLM Confers a Strong Protein–Protein Interaction. To gain more insight into the nature of the oligomerization and helicase activity transition of BLM, we next assayed to quantitatively measure the strength of the protein–protein interaction at the converged forks. To this end, following the stalled translocation of BLMs (Fig. 1*C*), we purposely disrupted the DNA tether by gradually increasing the applied force on that tether. The rupture force reflects the strength of the two ssDNA molecules bridged by the oligomeric BLM. To avoid the influence of Sytox on dsDNA elasticity (24), we used BLM-eGFP in this assay. Unexpectedly, more than half of the 36 stalled DNA tethers did not break, even after the overstretching transition of bead-attached dsDNA segments at a force of ∼65 pN (Fig. 3*A* and *SI Appendix*, Fig. S8) (25). It is noteworthy that this particular DNA tether can sustain a disruptive force of up to 300 pN, suggesting a strong linkage of two independent ssDNA molecules by the oligomeric BLM (Fig. 3*B*). In comparison, BLM at one fork junction can be easily disrupted at a significantly low force of 20.7 ± 1.1 pN (*SI Appendix*, Fig. S9). Thus, the strong interaction detected at the converged forks at least partially results from the protein–protein interaction.

Fork convergence and BLM oligomerization lead to the formation of a distinctive branched nucleic acid structure that contains four ssDNA arms joined together (Fig. 2*D*). The translocation of an oligomeric BLM on two ssDNA molecules actively mediates the change in the four ssDNA lengths. This particular ssDNA geometry, together with its dynamic transformation, resembles a well-known four-strand dsDNA structure: Holliday junction (HJ) (26). BLM is known for its capability to resolve this particular recombination intermediate with a requirement of the helicase and RNase D C-terminal (HRDC) domain (27). We next sought to address whether the detected onsite oligomerization and helicase activity transition necessitate the HRDC domain of BLM as well. We repeated the unwinding/translocation assay with an HRDC-depleted gBLM ($gBLM^{\Delta HRDC}$). Although smooth unwinding events initiated from both nicks were detected with this BLM mutant, 94% of the DNA tethers broke immediately after fork convergence ($n = 32$) (Fig. 3*C*). Similar results were also obtained with an HRDC-depleted hBLM core helicase ($hBLM^{\Delta HRDC}$) (*SI Appendix*, Fig. S10). These findings imply that the HRDC domain of BLM mediates the protein oligomerization and unwinding-translocation transition and further strengthen the conclusion that the protein–protein interactions at the converged forks confer the rate transition.

The Oligomeric BLM Is Capable of Dislodging SSBs. BLM, together with protein partners, plays multifaceted roles in the maintenance of genome integrity (19). This newly identified oligomerization and the unwinding-translocation transition of BLM possibly serve as a pathway to switch its cellular functions. Replication protein A (RPA), a eukaryotic SSB, not only physically and functionally interacts with BLM as a key partner protein, but also avidly binds to ssDNA to avoid damage in the physiological setting (28, 29). Therefore, we asked whether BLM could shift from dsDNA unwinding to counteract the loading of RPA on ssDNA after oligomerization at the forks. We labeled human RPA with eGFP (hRPA-eGFP) and, in its presence, repeated the BLM-mediated DNA unwinding/translocation assay. A microfluidic system was used for the rapid switching of experimental conditions (30). The unwinding assay was first initiated in a channel containing 200 nM BLM and 10 nM hRPA-eGFP under 30 pN. Note that we used a relatively low amount of RPA in this assay to attenuate the bidirectional unwinding of BLM from the nicks (20). As hRPA-eGFP coating on ssDNA allows for the direct visualization of unwinding intermediates of ssDNA, a kymograph of the DNA track directly showed two head-on unwinding events, as indicated by the hRPA-coated ssDNAs under tension between two nicks (Fig. 4*A*, Step 1). Meanwhile, unwound coiled ssDNAs located at the ends of the newly generated ssDNAs were also coated with hRPA-eGFP, as illustrated by

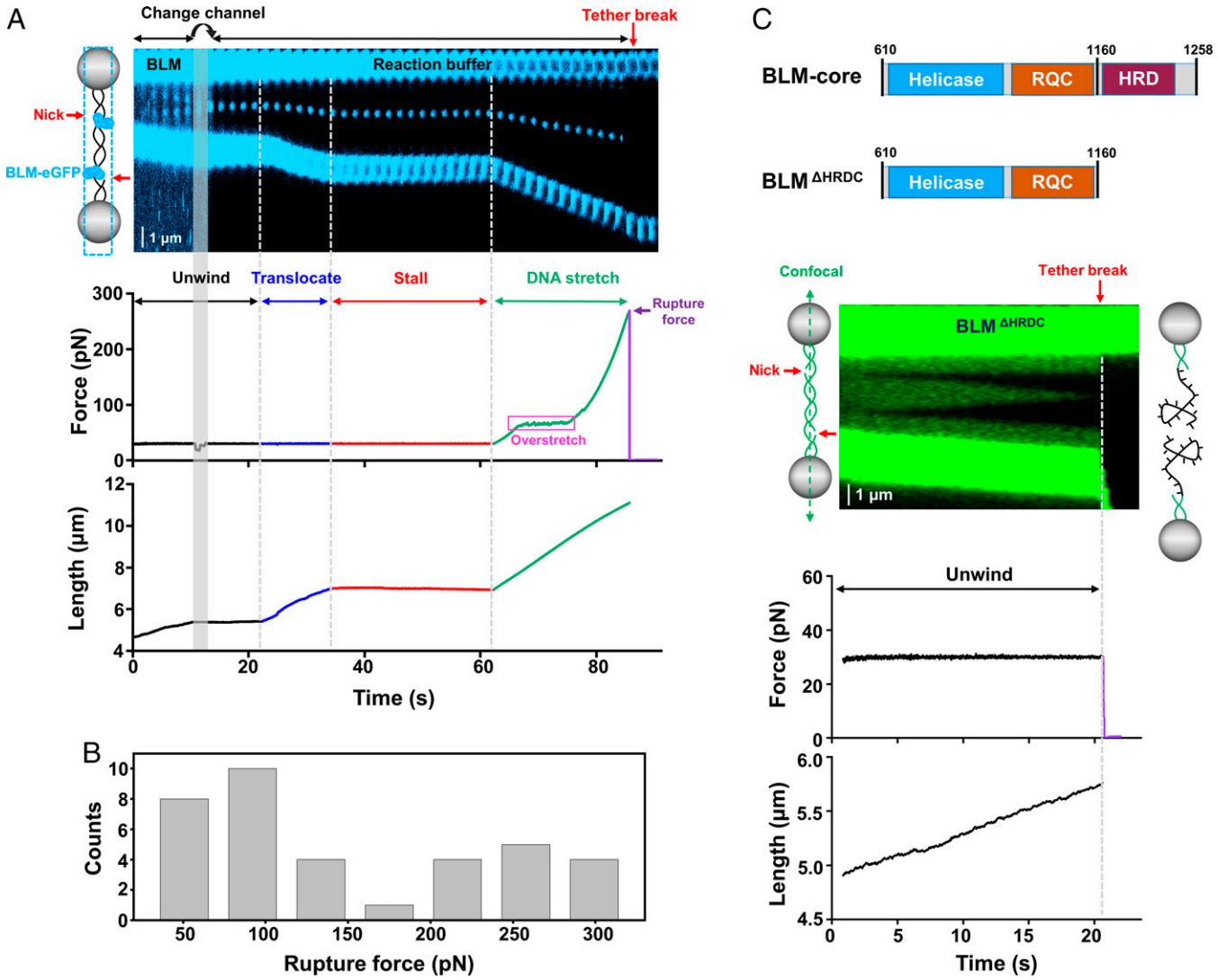

Fig. 3. Characteristics of the onsite oligomerization of BLM at the converged forks. (*A*) A representative kymograph of a double-nicked DNA as well as its corresponding force and length as a function of time in the reaction buffer with or without BLM-eGFP (cyan). The dsDNA unwinding was initiated in a channel containing 200 nM BLM-eGFP, after which the tether was transported to the reaction buffer (gray rectangle). In this buffer channel, BLMs unwind (black), oligomerize, translocate (blue), and stall (red). Next, the DNA tether was stretched until breakage (green). The pink rectangle indicates that dsDNA is overstretched, and the purple arrow indicates the breakage of the tether. (*B*) The distribution of rupture forces of the DNA tethers after stalls. (*C*) (*Top*) Schematic representations of BLM-core and BLM$^{\Delta HRDC}$. Helicase, RecQ C-terminal (RQC), and HRDC domains are shown in different colors. (*Bottom*) A representative kymograph of a tethered nicked DNA as well as its corresponding force and DNA length as a function of time in the presence of 200 nM BLM$^{\Delta HRDC}$ under 30 pN. The tether breakage is highlighted in purple.

the intense fluorescence signals. Following the convergence of two DNA unwinding forks, we immediately removed free proteins in the solution by transporting the DNA tether to a reaction buffer channel, wherein ATP was provided as a power source for helicase (Step 2). In this channel, an enhanced DNA extension, along with helicase activity transition, was detected (Fig. 4*A*) ($n = 25$). With the progression of the translocation of the oligomeric BLM, two dark regions flanking the fork junctions appeared and subsequently expanded. Meanwhile, the fluorescence intensities of the coiled ssDNAs correspondingly decreased. Simultaneous monitoring of both BLM (labeled with eGFP) and RPA (labeled with mCherry) confirmed that the RPA displacement arises from the translocation of the oligomeric BLM across the fork junctions (*SI Appendix*, Fig. S11). These findings suggest that an oligomeric BLM can translocate on hRPA-coated ssDNA under 30 pN, albeit at a reduced rate and processivity (Fig. 4 *C* and *D*), and the translocation actively stripped off the hRPA proteins on ssDNAs. Similar results were also produced under 10 and 20 pN, with reduced translocation rates but comparable translocation lengths of the oligomeric BLM (*SI Appendix*, Fig. S12).

In addition to prorecombinogenic activity, BLM can act as an anti-recombinase, disrupting potentially harmful homologous recombination (HR) intermediates formed by RAD51 to prevent illegitimate recombination (31, 32). However, the *in vitro* assay showed the inability of BLM to translocate to RAD51-coated ssDNA or displace RAD51 (33). The unique configuration formed by an oligomeric BLM on the fork junctions could strengthen its capability in the continuous translocation on ssDNA, thus actively dislodging loaded RAD51. To test this hypothesis, Alexa Fluor 555-labeled human RAD51 (hRAD51-AF555) protein was used. The stable assembly of active RAD51-ssDNA filaments requires the presence of both ATP and Ca^{2+}, and in addition to ssDNA, RAD51 can polymerize on dsDNA at a relatively slow rate (34, 35). Therefore, we started dsDNA unwinding in a channel containing 200 nM BLM, 2 mM Mg^{2+}, and 2 mM Ca^{2+} (Fig. 4*B*, Step 1). In this BLM channel, fork convergence and helicase translocation

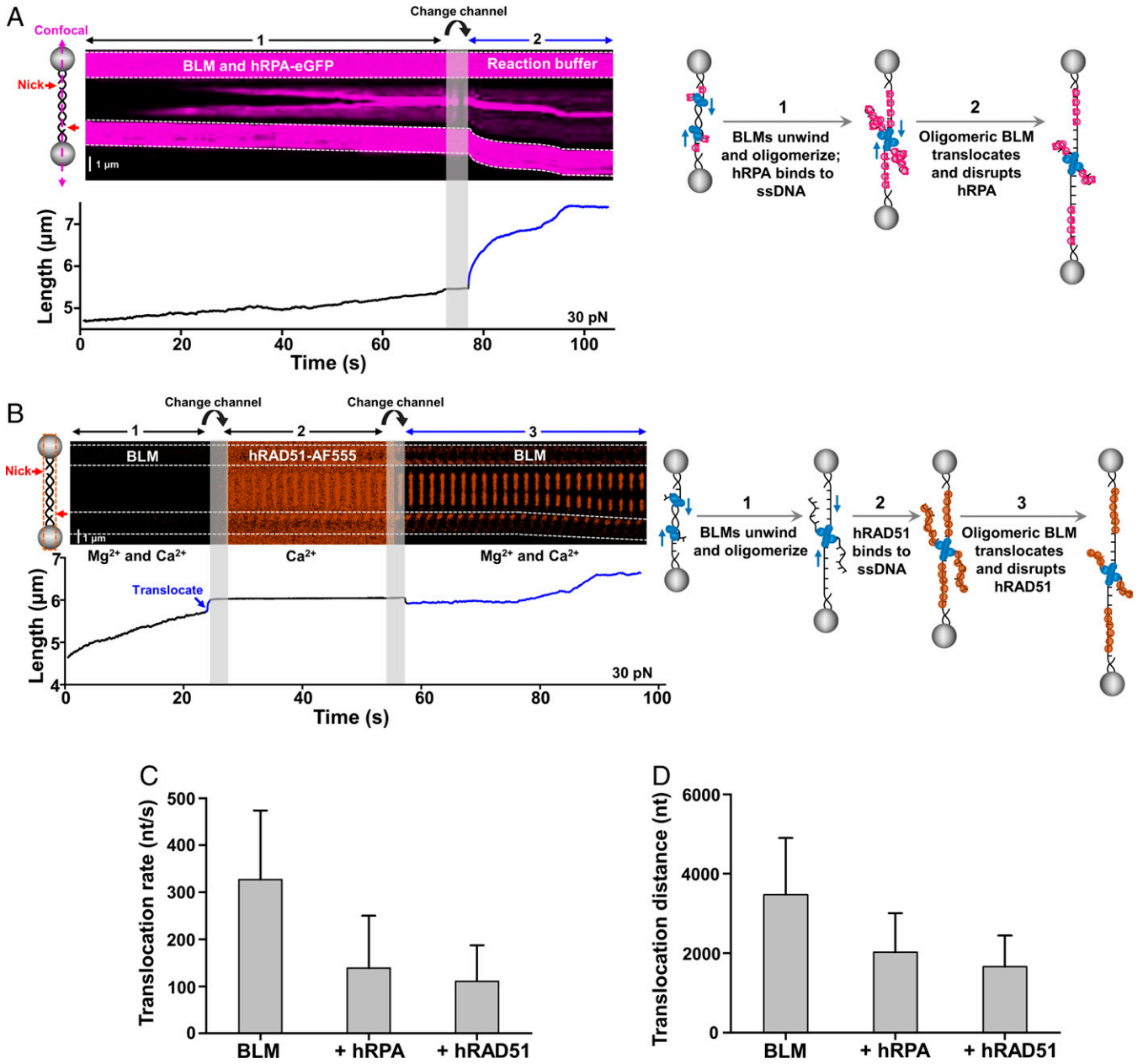

Fig. 4. The translocation of the oligomeric BLM along SSB-coated ssDNA. (*A*) Representative kymograph and DNA length versus time trace of a double-nicked tether showing dsDNA unwinding, ssDNA translocation, and hRPA displacement by BLM. The dsDNA unwinding of the nicked DNA template was initiated in a channel containing 200 nM BLM and 10 nM hRPA-eGFP under 30 pN (Step 1). Next, the DNA tether was quickly transported (gray rectangle) to a reaction buffer channel containing 2 mM ATP (Step 2). Tensioned and coiled ssDNAs were coated with hRPA-eGFP (purple). The horizontal dotted lines indicate the edges of the beads. (*Right*) The cartoon illustrates the progression of BLM unwinding dsDNA, oligomerization upon fork convergence, translocation along ssDNA, and disruption of hRPA. For clarity, only one helicase across each fork junction is shown in the cartoon. (*B*) Representative kymograph and DNA length versus time traces of a double-nicked DNA showing dsDNA unwinding, ssDNA translocation, and hRAD51 displacement by BLM. The dsDNA unwinding of the nicked DNA template was initiated in a channel containing 200 nM BLM, 2 mM Mg^{2+}, and 2 mM Ca^{2+} under 30 pN (Step 1). Next, the DNA tether was quickly transported (gray rectangle) to a channel containing 500 nM hRAD51-AF555 and 5 mM Ca^{2+} for a 20-s incubation (Step 2). The tether was then moved back (gray rectangle) to the original channel (Step 3). Tensioned ssDNAs were coated with hRAD51 (brown). (*Right*) The cartoon illustrates the progression of BLM unwinding dsDNA, oligomerization upon fork convergence, translocation along ssDNA, and disruption of hRAD51. (*C* and *D*) The ssDNA translocation rate in nt/s and distance in nt of the oligomeric BLM in the absence and presence of hRPA-eGFP or hRAD51-AF555 under 30 pN. The error bars represent SD.

occurred, as indicated by the transition of the DNA extension rate. Then, we immediately transported the tether to a channel containing 500 nM hRAD51-AF555, 2 mM ATP, and 5 mM Ca^{2+} (Step 2). In this channel, the DNA tether was incubated for a short period of 20 s, allowing for the stable coating of hRAD51 on ssDNA but not on dsDNA. Meanwhile, the deletion of Mg^{2+} in this channel abolished BLM-mediated dsDNA unwinding or ssDNA translocation. Note that unlike RPA-coated ssDNA, the unwound coiled ssDNA, once coated with hRAD51, becomes too stiff to be detected. Next, we resumed helicase translocation activity by transporting the tether back to the original channel containing ATP and Mg^{2+} as well as Ca^{2+} for the stable binding of hRAD51 to ssDNA (Step 3). In this channel, a relatively slow increase in DNA length and a gradual disappearance of the fluorescence signal of hRAD51 in the middle of the DNA track were monitored (Fig. 4*B*) ($n = 23$). Up to 65% of the traces examined ended up with stalled translocation. Similar observations were also made under lower

external forces of 10 and 20 pN, as well as in the presence of 5 mM Ca^{2+} (*SI Appendix*, Figs. S13 and S14). As demonstrated by the experiment that allowed for simultaneous monitoring of both BLM (labeled with eGFP) and hRAD51 (labeled with AF647), the disruption of the RAD51-ssDNA filament, indeed, arises from the translocation of the oligomeric BLM (*SI Appendix*, Fig. S15). Moreover, the dark regions flanking the fork junctions further corroborate the simultaneous translocation of both coiled ssDNAs by the oligomeric BLM. These results strongly suggest that an oligomeric BLM at converged forks can disrupt a stable form of the hRAD51-ssDNA filament, although the translocation rate and processivity of the oligomeric BLM were attenuated by the presence of hRAD51 (Fig. 4 *C* and *D*).

To exclude the possibility that the observed SSB displacement by gBLM was due to the heterologous combination, we also carried out DNA unwinding experiments using hBLM, and results similar to the heterologous combination were obtained (*SI Appendix*, Fig. S16).

Discussion

This work not only builds a relationship between the oligomeric state and activity of BLM, but also provides a distinct activity transition pathway for a DNA helicase. The convergence of head-on unwinding forks leads to the onsite fusion of two groups of BLM. This protein oligomerization, in turn, enhances the binding affinity of BLMs to the DNA substrate and makes it possible for BLMs to continuously translocate on ssDNAs and actively displace SSBs. This activity transition can be simply achieved via the alternation of DNA substrate configuration and takes place in a timely fashion. Our work is a direct observation of helicase activity transition induced by onsite oligomerization. Previous studies of the UvrD helicase have reported that dimerization is required to carry out efficient dsDNA unwinding, which is of a somewhat different nature than what we have observed in this work (10, 12).

Previous studies demonstrated that the helicase core of BLM is in the monomeric form (36, 37). Consistently, our chromatographic analysis revealed that the BLM-eGFP protein used in this work exists as monomers (*SI Appendix*, Fig. S17). Moreover, a kinetic study has proven that the monomeric BLM is responsible for dsDNA unwinding (15). However, the structural and single-molecule studies suggested that a dimeric BLM functionally acts on an HJ (18, 38). Therefore, there is a possibility that the BLM oligomerization detected in this work is realized by the dimerization of two monomeric unwinding BLMs across the forks. The fact that a few BLMs were detected near each unwinding fork could be reasoned by BLMs following the monomeric one and ensuring processive dsDNA unwinding. In support of this notion, the phenomenon of helicases trailing behind the lead one at the fork has been previously reported with other RecQ family helicases (39). Interestingly, the HRDC domain of BLM has been indicated to play a fundamental role in conferring its interactions with both ssDNA and HJ (27, 38). Our experiments also provided evidence for the indispensability of the HRDC domain in mediating converged unwinding forks. This domain may serve to provide a means to stabilize the branched ssDNA structure as well as the protein oligomerization/dimerization.

Our work exhibits a four-strand HJ-like ssDNA structure formed by an oligomeric helicase bridging two independent ssDNA molecules. This branched ssDNA structure may appear as an intermediate in HR-directed DNA double-strand break repair pathways. For instance, in the single-strand annealing (SSA) repair pathway, following DNA end resection that generates ssDNA, bridging of two homologous ssDNA sequences is involved. This particular DNA intermediate resembles the one reported in our work (40). Moreover, the break-induced replication (BIR) repair pathway relies on the invasion of a resected DNA into the dsDNA template, followed by a migrating bubble driving an unusual mode of DNA synthesis (41). The migration of a ssDNA junction in the joint molecule intermediate also shares a similarity with the dynamic movements of two ssDNA molecules mediated by BLM. Intriguingly, accumulating evidence suggests that BLM is involved in both the SSA and BIR pathways (42, 43). It is worth the effort to further inspect the *in vivo* existence of this distinctive DNA structure and to address whether the oligomeric BLM is the regulatory protein for the structure.

Our findings also constitute *in vitro* evidence for BLM's capability of displacing SSBs from ssDNA. In early HR repair, RPA coats along ssDNA to protect them from nucleolytic degradation (44). Subsequently, the displacement of RPA from ssDNA facilitates the formation of an extended helical filament of RAD51 on ssDNA, which catalyzes the pairing of the bound ssDNA with a homologous dsDNA target (45). Our findings imply that BLM may accelerate the formation of the RAD51-ssDNA filament by replacing RPA with RAD51. *In vivo* studies suggest that besides promoting DNA end resection, BLM is also an anti-recombinase that disrupts potentially harmful HR intermediates (31). Nevertheless, a DNA curtain-based approach demonstrated the inability of BLM to translocate along RAD51-coated ssDNA or remove SSBs *in vitro* (33). Our findings revealed that BLM oligomerization can potentiate its DNA binding affinity and, thus, ensure the disruption of the HR intermediates formed by RAD51. Whether the oligomeric BLM is responsible for the recognition of illegitimate HR intermediates is worthy of further exploration. Overall, our results provide a possible explanation for how BLM can act as both a pro- and anti-recombinase and play multiple functional roles in HR.

Materials and Methods

Protein Purification.

BLMs. WT *Gallus gallus* BLM was purified as previously described (46). *WT BLM* was amplified according to the NCBI reference sequence of BLM homolog. After digestion with EcoRI and SalI, the fragment was inserted into pET21a-SUMO (Takara) and then transformed into *E. coli* 2984 cells. Positive clones were identified by DNA sequencing, and the recombinant plasmid was transformed into *E. coli* ER2566 cells for overexpression. In general, cells harboring the expression vector were cultured in Luria–Bertani (LB) at 37 °C until OD600 arrived 0.6. The cells were then induced with 0.3 mM isopropylthio-β-galactoside (IPTG) at 18 °C for 16 h. The induced cells were harvested by centrifugation at 3,000 *g* for 10 min. Then, each cell pellet was resuspended with the corresponding ice-cold lysis buffer and crushed under high pressure (800 to 1,000 bar) three times. The supernatants were separated from the precipitants by centrifugation at 13,000 *g* for 30 min at 4 °C. Note that all BLMs and mutants were expressed similarly. WT BLM protein was bonded to the cOmplete His-tag purification resin (Roche) and then eluted by lysis buffer containing 300 mM imidazole. The elutes were digested with sumo protease at 18 °C for 4 h. At last, WT BLM was purified sequentially by HiTrap SP HP column (GE Healthcare) and HiTrap Q HP column (GE Healthcare).

The helicase-core fragment of gBLM (amino acid residues 610 to 1,258) and $BLM^{\Delta HRDC}$ (amino acid residues 610 to 1,160) were prepared as previously described (46). *BLM-core* was amplified from the *WT BLM* sequence. After digestion with NdeI and SalI, the *BLM-core* fragment was constructed into pTWIN1 (New England Biolabs, NEB) with a chitin binding domain tag by using NdeI and SalI restriction sites and transformed into *E. coli DH5α*. The positive plasmid

was confirmed by DNA sequencing and transformed into *E. coli* BL21 (DE3) competent cells. Protein was purified sequentially by chitin resin and tandem Q-SP HP column (GE Healthcare). The $BLM^{\Delta HRDC}$ protein was obtained similarly.

To obtain BLM-eGFP, the *BLM* gene was amplified and inserted into a pET28a expression vector, and the *eGFP* fragment was inserted at the N terminal of the BLM fragment through In-Fusion Cloning. The positive plasmid containing pET28a-BLM-eGFP was transformed into *E. coli* BL21 (DE3) and purified with Ni-NTA resin (TransGen). The resin was washed with the lysis buffer (50 mM Tris·HCl pH 7.5, 500 mM NaCl, 10% glycerol, 1 mM ethylenediaminetetraacetic acid [EDTA], and 0.1% Triton X-100) and then eluted stepwise with the same buffer containing 10, 20, 50, and 200 mM imidazole. The bulk of BLM-eGFP eluted in 50- and 200-mM imidazole steps. The protein was further purified by size-exclusion chromatography (Superdex 75 Increase 10/300 GL, GE Healthcare) with storage buffer (20 mM Tris·HCl pH7.5, 300 mM NaCl, 5% glycerol, 1 mM EDTA, and 1 mM dithiothreitol [DTT]) on an ÄKTA purifier (GE Healthcare).

hBLM-core (hBLM, amino acid residues 642 to 1,290) and $hBLM^{\Delta HRDC}$ (amino acid residues 642 to 1,192) were prepared as previously described (47). Briefly, the fragment of *hBLM* was inserted into the NdeI and XhoI cloning sites of the pET15b expression plasmid (Novagen), respectively. The resulting recombinant plasmid was transformed into *E. coli* BL21 (DE3) competent cells. The induced cells were harvested by centrifugation and resuspended in lysis buffer (20 mM Tris·HCl pH 7.9, 500 mM NaCl, 10% glycerol, 0.1% Triton X-100, and 1 mM phenylmethanesulfonyl fluoride [PMSF]). The soluble extract was applied to a 20-mL Ni-NTA resin (QIAGEN), and the resin was washed with the same buffer and then eluted stepwise with 50, 100, 200, 500, and 1,000 mM imidazole. The recombinant BLM protein was retained on the resin and recovered in the 200-mM imidazole eluate and further purified by fast performance liquid chromatography size-exclusion chromatography (Superdex 200, GE Healthcare). The $hBLM^{\Delta HRDC}$ protein was obtained similarly.

hRPA-eGFP and hRPA-mCherry. To obtain fluorescent hRPA, a DNA fragment of eGFP with a polyhistidine tag was inserted into the 3′ end of the complementary DNA encoding the large RPA70 subunit in the expression plasmid p11d-tRPA. The positive plasmid was transformed in *E. coli* Rosetta/pLysS cells (Novagen). The induced cells were incubated in LB at 37 °C until OD600 0.5 to 0.6. Then, the culture temperature was lowered to 15 °C for 16 h, and protein production was induced by the addition of 1 mM IPTG. hRPA-eGFP was purified by HiTrap FF and HiTrap Heparin HP columns as described previously (48). To purify hRPA-mCherry protein, the *RPA* gene was amplified from p11d-tRPA, digested by NheI and BamHI, and then inserted into pET28a to generate pET28a-RPA. The *mCherry* gene was amplified and inserted into the pET28a-RPA vector through In-Fusion Cloning. The fusion plasmid was transformed into *E. coli* BL21 (DE3). The induced cells were lysed and crushed in lysis buffer (20 mM Tris·HCl pH 7.5, 500 mM NaCl, 10% glycerol, 2 mM β-mercaptoethanol, and 5 mM imidazole), and the cleared cell lysates were incubated with Ni-NTA resin (TransGen) for 1 h at 4 °C. The resin was washed with the lysis buffer and then eluted stepwise with the lysis buffer containing 10, 20, 50, and 200 mM imidazole. The bulk of hRPA-mCherry eluted in 50- and 200-mM imidazole steps. The protein was further purified by HiTrap Heparin column.

hRAD51-AF555 and hRAD51-AF647. The human RAD51 open reading frame was subcloned between the NcoI and BamHI sites of pET11d (Novagen). There are five cysteine residues in human RAD51. Among them, Cys31 and Cys319 are exposed to solvents according to structural predictions. To obtain a homogeneous population of RAD51 monomers with fluorescent labels, we mutated Cys319 to Ser by the QuikChange Site-Directed Mutagenesis method. The detailed labeling procedures of RAD51 were described previously (48, 49). Briefly, the concentration of DTT was adjusted to 20 mM in the purified RAD51 samples (at 1 to 2 mg/mL RAD51) and incubated for 30 min on ice. The sample was buffer exchanged into labeling buffer (50 mM 3-(*N*-morpholino)propanesulfonic acid-HCl pH 7.0, 300 mM KCl, 1 mM EDTA, 10% glycerol, degassed with argon for 30 min before use). The maleimide-coupled Alexa Fluor 555 or 647 dye (Molecular Probes) was resuspended in labeling buffer just prior to use and immediately added to the protein sample at a 10-fold molar excess (dye/RAD51) while mixing. The reaction was incubated on ice for 30 min and quenched by the addition of DTT to 20 mM with further 30 min incubation on ice. Excess dye was removed by buffer exchange into 0.3 M KCl, 50 mM Tris·HCl pH 7.5, 1 mM EDTA, 2 mM DTT, and 10% glycerol.

dSaCas9 and sgRNA. The dSaCas9 protein was purified as previously described (50). Briefly, a synthetic gene coding for dSaCas9 with an N-terminal His-tag was generated, followed by a peptide sequence containing a tobacco etch virus protease cleavage site. The sequence was synthesized and subcloned into pET28a to generate pET28a-dSaCas9. Proteins were expressed in the *E. coli* strain BL21(DE3) (TransGen) grown in LB at 37 °C until OD600 0.5 to 0.6. Then, the culture temperature was lowered to 18 °C, and protein production was induced by the addition of 200 μM IPTG. The harvested cells were lysed in 20 mM Tris·HCl pH 8.0, 250 mM NaCl, 5 mM imidazole pH 8.0, and 1 mM PMSF and passed through the homogenizer three times. The lysed dilution was then ultracentrifuged, and the supernatant-clarified cell lysate was separated from the cellular debris and bound in batches to Ni-NTA agarose. The resin was washed extensively with 20 mM Tris·HCl pH 8.0, 250 mM NaCl, and 10 mM imidazole pH 8.0, and the bound protein was eluted in a single step with 20 mM Tris·HCl pH 8.0, 250 mM NaCl, and 250 mM imidazole pH 8.0. dSaCas9 was further purified by a HiTrap SP HP Sepharose column (GE Healthcare) and by gel-filtration chromatography on a Superdex 200 16/60 column (GE Healthcare) and was stored at −80 °C.

The sgRNA was transcribed from linearized pUC57-sgRNA expression vectors using the T7 High-Efficiency Transcription Kit (TransGen). The sgRNA was then purified by the EasyPure RNA Purification Kit (TransGen). The DNA target sequence is 5′- GGA ACC TCT TGC AGT ACT ACT G -3′.

DNA Template Preparation.

Nicked dsDNA. The 13.8-kbp DNA template containing two nicks is composed of three DNA segments connected by two short dsDNA adaptors, 1 and 2 (*SI Appendix*, Fig. S1). Two 4.0-kbp dsDNA segments were PCR amplified from the lambda DNA (Thermo) using biotin-labeled primers (*SI Appendix*, Table S1). A 5.8-kbp dsDNA unwinding segment was PCR amplified from the lambda DNA. The three resulting DNA fragments were all digested with BstXI (NEB) to create an overhang. The adaptors were produced by annealing two oligonucleotides, one of which misses the 5′ phosphate, allowing for the automatic generation of the nicks after the ligation (*SI Appendix*, Table S1). Two adaptors were first ligated with the 5.8-kbp DNA segment, and then the ligation product was purified. The final product was produced by ligating the two 4.0-kbp DNA segments and the 5.8-kbp DNA fragment with the adaptors at a 3:3:1 ratio using T4 ligase (NEB).

Intact dsDNA. The 8.3-kbp DNA template used for generating ssDNA was PCR amplified from the lambda DNA using biotin-labeled primers (*SI Appendix*, Fig. S2 and Table S1). The PCR product was first digested with EcoRI (NEB). The complementary nucleotides biotin-14-dATP and dTTP (Invitrogen) were incorporated into these overhangs. In this way, the DNA molecule was labeled with biotin on both ends of the same strand. Force-induced dsDNA melting results in the release of the unlabeled strand of the tethered dsDNA, thus yielding a tethered ssDNA molecule (*SI Appendix*, Fig. S2*D*) (51). To this aim, the dsDNA was first extended beyond overstretching to 70 to 80 pN for 5 to 10 s, allowing the dsDNA to melt. A ssDNA sample was verified by its inherent mechanical force-extension curve (25).

Single-Molecule Experiments and Data Analysis. Single-molecule experiments were performed at 25 °C on an instrument combining three-color confocal fluorescence microscopy with dual optical traps (LUMICKS C-trap, Netherland). In brief, a 1,064-nm laser and a water-immersion objective were used to create two orthogonally polarized optical traps. The trap separation was controlled using a piezo mirror for beam-steering one trap. Force measurements were performed by back-focal plane interferometry of the condenser top lens using a position-sensitive detector. A computer-controlled stage enabled rapid movement of the optical traps within a multiple-channel laminar flow cell, which allows for rapid and complete buffer change (52). DNA molecules were captured between two streptavidin-coated polystyrene beads (1.76-μm diameter, Spherotech) using the multichannel laminar flow cell and were tensioned by increasing the length between the optical traps. All channels of the flow cell were first passivated with casein (1% wt/vol in PBS). A single DNA sample was verified by its inherent mechanical force-extension curve (25). Then, the tethered DNA was moved to protein channels as described for specified assays. The typical BLM reaction buffer contains 25 mM Tris·HCl pH 7.5, 100 mM NaCl, 1 mM $MgCl_2$, 0.1 mg/mL bovine serum albumin, 2 mM ATP, and 3 mM DTT. To obtain fluorescence signals, 488-, 532-, and 638-nm excitation lasers were used, and the emission was detected with a photon-counting avalanche photodiode. Confocal

pixel size was set to 75 nm. The pixel dwell time was 0.5 ms for eGFP, mCherry, and AF647 detection and 0.2 ms for Sytox and AF555 detection. The interframe wait time was 200 ms for the line scanning and 500 ms for the rectangular scanning.

Force, DNA extension, and fluorescence data were analyzed using custom software provided by LUMICKS. Pseudocolor was used by Zen 3.2 software (Zeiss) for better visualization of the signal contrast. DNA force and extension data were taken at 100 Hz. DNA unwinding and translocation rates were measured from fitting to the linear region of the length versus time traces. Since there was a significant difference between the unwinding rate and the translocation rate, a first-order derivative was used to determine the transition point from unwinding to translocation. The dsDNA unwinding length before the rate transition was calculated based on the difference between the original length of the nicked dsDNA and the DNA length at the transition point under a specific force. For converting dsDNA or ssDNA extension to the number of base pairs or nucleotides, the force-extension relation of dsDNA was obtained by stretching the nicked dsDNA under the same reaction buffer and was fit to extendible worm-like-chain model (*SI Appendix*, Fig. S2 *A–C*) (53). Long ssDNA molecules were generated by overstretching and melting an 8.3-kbp dsDNA molecule. The force-extension relation of ssDNA in the reaction buffer was then obtained and fit to the freely jointed-chain model (*SI Appendix*, Fig. S2 *D–F*) (25). Based on the elastic parameters of dsDNA and ssDNA under different conditions, the DNA length in nm was converted to bp or nt, and the dsDNA unwinding rate in nm/s and ssDNA translocation rate in nm/s were converted to bp/s and nt/s, respectively. The unwinding and translocation rates and processivities were reported as the mean ± SD from the indicated number of events.

Data Availability. All study data are included in the article and/or *SI Appendix*.

ACKNOWLEDGMENTS. We thank all the staff of the molecular and cell biology core facility of the School of Life Science and Technology at ShanghaiTech University for providing technical support. This work was supported by the National Natural Science Foundation of China (32022048 to B.S. and 32100993 to L.B.), the Natural Science Foundation of Shanghai (19ZR1434100 and 22ZR1441900 to B.S.), and ShanghaiTech University Startup funding (to B.S.). M.M. is supported by the French National Cancer Institute, the French National Research Agency, and the French National League Against Cancer (équipe labellisée).

Author affiliations: [a]School of Life Science and Technology, ShanghaiTech University, Shanghai 201210, China; [b]CAS Center for Excellence in Molecular Cell Science, Shanghai Institute of Biochemistry and Cell Biology, Chinese Academy of Sciences, Shanghai 200031, China; [c]University of Chinese Academy of Sciences, Beijing 100049, China; [d]College of Life Sciences, Northwest A&F University, Yangling 712100, China; [e]Cancer Research Center of Marseille, CNRS UMR7258, Inserm U1068, Institut Paoli-Calmettes, Aix-Marseille Université, 13273 Marseille, France; and [f]Université Paris-Saclay, ENS Paris-Saclay, CNRS, LBPA, 91190 Gif-sur-Yvette, France

1. R. M. Brosh Jr., S. W. Matson, History of DNA helicases. *Genes (Basel)* **11**, 255 (2020).
2. T. M. Lohman, K. P. Bjornson, Mechanisms of helicase-catalyzed DNA unwinding. *Annu. Rev. Biochem.* **65**, 169–214 (1996).
3. I. Jarmoskaite, R. Russell, RNA helicase proteins as chaperones and remodelers. *Annu. Rev. Biochem.* **83**, 697–725 (2014).
4. A. M. Pyle, Translocation and unwinding mechanisms of RNA and DNA helicases. *Annu. Rev. Biophys.* **37**, 317–336 (2008).
5. S. S. Patel, K. M. Picha, Structure and function of hexameric helicases. *Annu. Rev. Biochem.* **69**, 651–697 (2000).
6. M. R. Singleton, M. S. Dillingham, D. B. Wigley, Structure and mechanism of helicases and nucleic acid translocases. *Annu. Rev. Biochem.* **76**, 23–50 (2007).
7. T. M. Lohman, E. J. Tomko, C. G. Wu, Non-hexameric DNA helicases and translocases: Mechanisms and regulation. *Nat. Rev. Mol. Cell Biol.* **9**, 391–401 (2008).
8. Y. Gao, W. Yang, Different mechanisms for translocation by monomeric and hexameric helicases. *Curr. Opin. Struct. Biol.* **61**, 25–32 (2020).
9. R. M. Brosh, Jr, DNA helicases involved in DNA repair and their roles in cancer. *Nat. Rev. Cancer* **13**, 542–558 (2013).
10. B. Sun *et al.*, Impediment of *E. coli* UvrD by DNA-destabilizing force reveals a strained-inchworm mechanism of DNA unwinding. *EMBO J.* **27**, 3279–3287 (2008).
11. Y. Yang *et al.*, Evidence for a functional dimeric form of the PcrA helicase in DNA unwinding. *Nucleic Acids Res.* **36**, 1976–1989 (2008).
12. K. S. Lee, H. Balci, H. Jia, T. M. Lohman, T. Ha, Direct imaging of single UvrD helicase dynamics on long single-stranded DNA. *Nat. Commun.* **4**, 1878 (2013).
13. M. E. Fairman-Williams, U. P. Guenther, E. Jankowsky, SF1 and SF2 helicases: Family matters. *Curr. Opin. Struct. Biol.* **20**, 313–324 (2010).
14. N. J. Marianayagam, M. Sunde, J. M. Matthews, The power of two: Protein dimerization in biology. *Trends Biochem. Sci.* **29**, 618–625 (2004).
15. Y. N. Xu *et al.*, Multimeric BLM is dissociated upon ATP hydrolysis and functions as monomers in resolving DNA structures. *Nucleic Acids Res.* **40**, 9802–9814 (2012).
16. W. K. Chu, I. D. Hickson, RecQ helicases: Multifunctional genome caretakers. *Nat. Rev. Cancer* **9**, 644–654 (2009).
17. J. K. Karow, R. H. Newman, P. S. Freemont, I. D. Hickson, Oligomeric ring structure of the Bloom's syndrome helicase. *Curr. Biol.* **9**, 597–600 (1999).
18. M. Gyimesi *et al.*, Visualization of human Bloom's syndrome helicase molecules bound to homologous recombination intermediates. *FASEB J.* **27**, 4954–4964 (2013).
19. D. L. Croteau, V. Popuri, P. L. Opresko, V. A. Bohr, Human RecQ helicases in DNA repair, recombination, and replication. *Annu. Rev. Biochem.* **83**, 519–552 (2014).
20. Z. Qin *et al.*, Human RPA activates BLM's bidirectional DNA unwinding from a nick. *eLife* **9**, e54098 (2020).
21. S. Zhang *et al.*, Dynamics of *Staphylococcus aureus* Cas9 in DNA target Association and Dissociation. *EMBO Rep.* **21**, e50184 (2020).
22. D. E. Kim, M. Narayan, S. S. Patel, T7 DNA helicase: A molecular motor that processively and unidirectionally translocates along single-stranded DNA. *J. Mol. Biol.* **321**, 807–819 (2002).
23. D. S. Johnson, L. Bai, B. Y. Smith, S. S. Patel, M. D. Wang, Single-molecule studies reveal dynamics of DNA unwinding by the ring-shaped T7 helicase. *Cell* **129**, 1299–1309 (2007).
24. A. S. Biebricher *et al.*, The impact of DNA intercalators on DNA and DNA-processing enzymes elucidated through force-dependent binding kinetics. *Nat. Commun.* **6**, 7304 (2015).
25. S. B. Smith, Y. Cui, C. Bustamante, Overstretching B-DNA: The elastic response of individual double-stranded and single-stranded DNA molecules. *Science* **271**, 795–799 (1996).
26. J. K. Karow, A. Constantinou, J. L. Li, S. C. West, I. D. Hickson, The Bloom's syndrome gene product promotes branch migration of Holliday junctions. *Proc. Natl. Acad. Sci. U.S.A.* **97**, 6504–6508 (2000).
27. L. Wu *et al.*, The HRDC domain of BLM is required for the dissolution of double Holliday junctions. *EMBO J.* **24**, 2679–2687 (2005).
28. R. M. Brosh Jr. *et al.*, Replication protein A physically interacts with the Bloom's syndrome protein and stimulates its helicase activity. *J. Biol. Chem.* **275**, 23500–23508 (2000).
29. M. S. Wold, Replication protein A: A heterotrimeric, single-stranded DNA-binding protein required for eukaryotic DNA metabolism. *Annu. Rev. Biochem.* **66**, 61–92 (1997).
30. A. Candelli, G. J. L. Wuite, E. J. G. Peterman, Combining optical trapping, fluorescence microscopy and micro-fluidics for single molecule studies of DNA-protein interactions. *Phys. Chem. Chem. Phys.* **13**, 7263–7272 (2011).
31. D. S. Patel, S. M. Misenko, J. Her, S. F. Bunting, BLM helicase regulates DNA repair by counteracting RAD51 loading at DNA double-strand break sites. *J. Cell Biol.* **216**, 3521–3534 (2017).
32. D. V. Bugreev, X. Yu, E. H. Egelman, A. V. Mazin, Novel pro- and anti-recombination activities of the Bloom's syndrome helicase. *Genes Dev.* **21**, 3085–3094 (2007).
33. C. Xue *et al.*, Single-molecule visualization of human BLM helicase as it acts upon double- and single-stranded DNA substrates. *Nucleic Acids Res.* **47**, 11225–11237 (2019).
34. D. V. Bugreev, A. V. Mazin, Ca^{2+} activates human homologous recombination protein Rad51 by modulating its ATPase activity. *Proc. Natl. Acad. Sci. U.S.A.* **101**, 9988–9993 (2004).
35. J. van Mameren *et al.*, Counting RAD51 proteins disassembling from nucleoprotein filaments under tension. *Nature* **457**, 745–748 (2009).
36. P. Janscak *et al.*, Characterization and mutational analysis of the RecQ core of the bloom syndrome protein. *J. Mol. Biol.* **330**, 29–42 (2003).
37. J. Shi *et al.*, A helical bundle in the N-terminal domain of the BLM helicase mediates dimer and potentially hexamer formation. *J. Biol. Chem.* **292**, 5909–5920 (2017).
38. X. Chen *et al.*, Uncovering an allosteric mode of action for a selective inhibitor of human Bloom syndrome protein. *eLife* **10**, e65339 (2021).
39. B. Rad, A. L. Forget, R. J. Baskin, S. C. Kowalczykowski, Single-molecule visualization of RecQ helicase reveals DNA melting, nucleation, and assembly are required for processive DNA unwinding. *Proc. Natl. Acad. Sci. U.S.A.* **112**, E6852–E6861 (2015).
40. R. Bhargava, D. O. Onyango, J. M. Stark, Regulation of single-strand annealing and its role in genome maintenance. *Trends Genet.* **32**, 566–575 (2016).
41. X. Wu, A. Malkova, Break-induced replication mechanisms in yeast and mammals. *Curr. Opin. Genet. Dev.* **71**, 163–170 (2021).
42. M. Kappeler, E. Kranz, K. Woolcock, O. Georgiev, W. Schaffner, *Drosophila* bloom helicase maintains genome integrity by inhibiting recombination between divergent DNA sequences. *Nucleic Acids Res.* **36**, 6907–6917 (2008).
43. J. R. Lydeard, Z. Lipkin-Moore, S. Jain, V. V. Eapen, J. E. Haber, Sgs1 and Exo1 redundantly inhibit break-induced replication and de novo telomere addition at broken chromosome ends. *PLoS Genet.* **6**, e1000973 (2010).
44. H. Chen, M. Lisby, L. S. Symington, RPA coordinates DNA end resection and prevents formation of DNA hairpins. *Mol. Cell* **50**, 589–600 (2013).
45. M. Sinha, C. L. Peterson, A Rad51 presynaptic filament is sufficient to capture nucleosomal homology during recombinational repair of a DNA double-strand break. *Mol. Cell* **30**, 803–810 (2008).
46. J. Shi, N. N. Liu, Y. T. Yang, X. G. Xi, Purification and enzymatic characterization of *Gallus gallus* BLM helicase. *J. Biochem.* **162**, 183–191 (2017).
47. R. B. Guo, P. Rigolet, L. Zargarian, S. Fermandjian, X. G. Xi, Structural and functional characterizations reveal the importance of a zinc binding domain in Bloom's syndrome helicase. *Nucleic Acids Res.* **33**, 3109–3124 (2005).
48. M. Modesti, Fluorescent labeling of proteins. *Methods Mol. Biol.* **1665**, 115–134 (2018).
49. M. Modesti *et al.*, Fluorescent human RAD51 reveals multiple nucleation sites and filament segments tightly associated along a single DNA molecule. *Structure* **15**, 599–609 (2007).
50. H. Nishimasu *et al.*, Crystal structure of *Staphylococcus aureus* Cas9. *Cell* **162**, 1113–1126 (2015).
51. A. Candelli *et al.*, A toolbox for generating single-stranded DNA in optical tweezers experiments. *Biopolymers* **99**, 611–620 (2013).
52. P. Gross, G. Farge, E. J. Peterman, G. J. Wuite, Combining optical tweezers, single-molecule fluorescence microscopy, and microfluidics for studies of DNA-protein interactions. *Methods Enzymol.* **475**, 427–453 (2010).
53. T. Odijk, Stiff chains and filaments under tension. *Macromolecules* **28**, 7016–7018 (1995).